Adsorption/Combustion-type Gas Sensors Employing Mesoporous γ-Alumina Loaded with Core(Au)/Shell(Pd) Nanoparticles Synthesized by Sonochemical Reduction

Takeo Hyodo[1,*], Yasunari Yuzuriha[1], Osamu Nakagoe[1], Takahiko Sasahara[2], Shuji Tanabe[1] and Yasuhiro Shimizu[1]

[1]Graduate School of Engineering, Nagasaki University, 1-14 Bunkyo-machi, Nagasaki 852-8521, Japan

[2]Yazaki Corporation, 1500 Mishuku, Susono, Shizuoka 410-1194, Japan

*Corresponding author:

Takeo Hyodo, Dr.

Graduate School of Engineering, Nagasaki University

1-14 Bunkyo-machi, Nagasaki 852-8521, Japan

Tel: +81-95-819-2644

Fax: +81-95-819-2643

E-mail: hyodo@nagasaki-u.ac.jp

Abstract

Adsorption/combustion-type gas sensors employing mesoporous γ-alumina (mp-Al_2O_3) powders loaded with core(Au)/shell(Pd) nanoparticles, which were synthesized by sonochemical reduction, (*n*(Au/Pd)/mp-Al_2O_3, *n*: the amount of Au/Pd nanoparticles loaded, *0.1~1.0* (wt%), Au : Pd = 1 : 4 in weight) have been fabricated and their sensing properties to ethanol, toluene and *n*-hexane have been investigated in air. The *n*(Au/Pd)/mp-Al_2O_3 sensors showed larger responses to these target gases at lower temperatures than those of sensors fabricated with mp-Al_2O_3 powders loaded with Au and Pd by general impregnation technique (*n*(Au-Pd)/mp-Al_2O_3 sensors, Au : Pd = 1 : 4 in weight), especially when the amount of Au and Pd loaded onto the mp-Al_2O_3 powders was reduced (≤ 0.5 wt%). These sensing properties seem to be largely dependent on the morphological and compositional characteristics of Au and Pd loaded on the γ-alumina surface. In addition, the *n*(Au/Pd)/mp-Al_2O_3 sensors showed much larger response to ethanol than those to toluene and *n*-hexane, probably because of the difference in the magnitude of polarity (dipole moment and dielectric constant) of their molecules. However, the sensors obviously detected even 10 ppm *n*-hexane with the extremely low dipole moment and dielectric constant. These results promise that the *n*(Au/Pd)/mp-Al_2O_3 sensors can detect the lower concentration of these gases as well as other VOCs.

***Keywords*:** adsorption/combustion-type gas sensor; palladium; gold; core-shell nanoparticles; sonochemical reduction; alcohol; toluene; *n*-hexane

1. Introduction

Volatile organic compounds (VOCs) were well-known as one of typical substances responsible for sick building syndrome such as headache, irritation of eyes, nose or throat, dizziness and nausea [1, 2]. The VOCs were continuously volatilized from new building materials and furniture fabricated with paints, adhesives and other petroleum products and so on, and thus it is very dangerous for the vast majority of human beings to be exposed to even a limited amount of VOCs in recent houses and buildings with high heat insulation as well as high air-tightness. To detect and then to eliminate these gases, therefore, the development of high performance gas sensors with high sensitivity were indispensable [3, 4].

Development on various types of VOC sensors have recently been attempted by many researchers [5-10]. We have also developed adsorption/combustion-type VOC sensors during the past decade [11-16]. The sensors are very promising to detect quite a low concentration of VOCs in comparison with other types of gas sensors, because the large amount of VOC molecules were firstly adsorbed on the surface of the sensor materials at lower temperatures and their dynamic combustion with abruptly rising temperature by pulse heating (general heat-up time: several-tens of milliseconds) realized the large response of the sensors to the VOC's. However, optimal, compositional and morphological controls of noble-metal catalysts loaded on the base sensor materials (generally, γ-alumina with large surface area and high thermal conductivity) were very indispensable to burn the VOCs adsorbed on the surface effectively and then to enhance the sensor response to the VOCs. Our previous studies have demonstrated that mesoporous γ-Al_2O_3 (mp-Al_2O_3) powders with a large surface area, which were prepared by microwave-assisted solvothermal technique employing aluminum secondary butoxide and behenic acid (mesopore template), were promising as the base sensor material, and the co-loading of the appropriate amount of 2 wt% Au and 8 wt% Pd nanoparticles on the mp-Al_2O_3 powders by impregnation technique drastically improved the sensing properties to ethanol of

adsorption/combustion-type gas sensors [15, 16]. In addition, the addition of thermally conductive α-Al_2O_3 powders to the sensor materials (mp-Al_2O_3 powders loaded with Au and Pd nanoparticles) was quite effective in improving the VOC sensing properties [16]. In this study, therefore, we have attempted to further improve VOC-sensing properties of the adsorption/combustion-type gas sensors by the highly-dispersive loading of core(Au)/shell(Pd) nanoparticles synthesized by sonochemical reduction [17-19] onto the surface of the mp-Al_2O_3 powders.

2. Experimental

2.1 Synthesis of core(Au)/shell(Pd) nanoparticles by sonochemical reduction

3.7 cm^3 of a 10 mM $PdCl_2 \cdot 2NaCl$ aqueous solution, 0.5 cm^3 of a 10 mM $HAuCl_4$ aqueous solution and 10 cm^3 of a 4 mM polyethylene glycol monostearate ($C_{17}H_{35}CO(CH_2CH_2O)_{40}OH$) aqueous solution were mixed with 57 cm^3 of de-ionized water. The precursor solution obtained was irradiated with strong ultrasonic wave (200 kHz, 6 W cm^{-2}) at 20°C for 30 min in a container filled with argon, and then the colloidal aqueous solution containing core(Au)/shell(Pd) (Au/Pd) nanoparticles (Au : Pd = 1 : 4 in weight (composition ratio for preparation)) was obtained in this container [17-19].

2.2 Preparation of mesoporous (mp-) Al_2O_3 powders

4.2 x 10^{-2} mol of aluminum secondary butoxide (Al(*sec*-$OC_4H_9)_3$) as an Al source and 8.4 x 10^{-3} mol of behenic acid ($C_{21}H_{43}COOH$) as a template were mixed with 4.0 mol of 1-propanol. After 10 cm^3 of pure water was added to the solution, it was stirred at room temperature for 45 h to hydrolyze Al(*sec*-$OC_4H_9)_3$. Then, the solution was treated at 110°C for 1 h by a solvothermal method (CEM Corp., MARS5). White precipitates obtained were centrifuged at a speed of 2500 rpm for 10 min, washed with ethanol and then fired at 700°C for 2 h in air [15, 16].

2.3 Loading with Au/Pd nanoparticles onto the surface of mp-Al_2O_3 powders

The appropriate amount of the mp-Al_2O_3 powders obtained was added into the colloidal aqueous solution containing the Au/Pd nanoparticles, and then the pH was adjusted to about 4. After the Au/Pd nanoparticles were adsorbed on the surface of the mp-Al_2O_3 powders, the powders obtained were filtered and dried at 40°C for 12 h. The obtained mp-Al_2O_3 powders loaded with Au/Pd were denoted as *n*(Au/Pd)/mp-Al_2O_3 (*n*: the amount of Au/Pd nanoparticles loaded, *0.1~1.0* (wt%)).

For comparative purpose, mp-Al_2O_3 powders loaded with Au and Pd were also prepared by a conventional impregnation method [15, 16]. The mp-Al_2O_3 powders were added into an aqueous solution containing various concentrations of $Pd(NO_3)_2$ and $HAuCl_4$. After the suspensions obtained were ultrasonicated at RT for ca. 15 min (24, 31, and 100 kHz, each for 5 minutes), they were dried on a magnetic hotplate stirrer. And then, the powders obtained were fired at 350°C for 1 h under a H_2 stream. The obtained mp-Al_2O_3 powders co-loaded with Au and Pd by the conventional impregnation method (Au : Pd = 1 : 4 in weight (composition ratio for preparation)) were denoted as *n*(Au-Pd)/mp-Al_2O_3 (*n*: the amount of Au-Pd nanoparticles loaded, *0.1~1.0* or *10* (wt%)).

2.4 Characterizations of gas-sensing materials

Particle-size distribution and ultraviolet and visible (UV-VIS) absorption spectra of Au/Pd nanoparticles synthesized by sonochemical reduction were estimated by dynamic light scattering (DLS; Malvern Instrument Ltd., HPPS) and UV-VIS spectroscopy (Jasco, V-650), respectively. Zeta potential of Au/Pd nanoparticles and mp-Al_2O_3 powders was measured by electrophoretic light scattering (ELS; Otsuka Electronics Co., Ltd., ELS-7000). Crystal structure of all powders was characterized by X-ray diffraction (XRD; Rigaku Corp., RINT2200, CuKα). Pore size distribution and specific surface area (SSA) of all powders were measured by Barrett–Joyner–Halenda (BJH) and Brunauer–Emmett–Teller (BET) methods

using a N_2 adsorption/desorption isotherm (Micromeritics Instruments Corp., Tristar3000), respectively. Microstructure and composition of all samples were observed by transmission electron microscopy (TEM; JEOL Ltd., JEM2010) and energy dispersive spectroscopy (EDS; Oxford, Lind ISIS) equipped with the TEM, respectively.

2.5 Sensor fabrication

Schematic drawings of the adsorption/combustion-type gas sensor fabricated were shown in Fig. 1(a). The *n*(Au/Pd)/mp-Al_2O_3 or *n*(Au-Pd)/mp-Al_2O_3 powder obtained was mixed with an organic vehicle (a mixed solution of 36.4 g of di-*n*-butyl phthalate and 53.6 g of terpineol containing 10 g of polyvinyl butyral resin (mean polymerization degree: 700)) at a concentration of ca. 20 wt%, followed by ball milling for 30 min. The pastes containing mp-Al_2O_3, *n*(Au/Pd)/mp-Al_2O_3 or *n*(Au-Pd)/mp-Al_2O_3 powder were applied on a micro-sensor chip fabricated by micro-electro-mechanical system (MEMS) technique, as a sensing or a reference film, respectively, by utilizing a fluid dispenser (Musashi Eng., In., MS-10DX) with a suitable size of syringe, and then the micro-sensor chips attached with these films were fired at 700°C for 2 h in air.

2.6 Gas-sensing properties of adsorption/combustion-type gas sensors

Gas-sensing properties of adsorption/combustion-type gas sensors fabricated were measured in an acrylic chamber (inner volume: 50 dm^3), in which an appropriate amount of a target gas (ethanol, toluene or *n*-hexane) was evaporated with a compact heater. A bridge circuit containing the micro-sensor chip, which was used to get output signals from the sensors, was shown in Fig. 1(b). The bridge was composed of a sensing film and a reference film on a micro-sensor chip, together with two fixed resistive elements. All sensors were operated with a mode of pulse-driven heating for 0.4 sec with a cycle of 10 sec, and the heating temperatures were preset at 250, 350 and 450°C. During the heater-off period for 9.6 sec, target-gas molecules in air adsorb on both the sensing and reference materials. Figure 2 shows a typical sensor-signal

profile of adsorption/combustion-type gas sensors. Upon pulse heating for 0.4 s, it is expected that the molecules adsorbed on the sensing material (*n*(Au/Pd)/mp-Al_2O_3 or *n*(Au-Pd)/mp-Al_2O_3) burn to induce a temperature increase, while those on the inactive reference material (mp-Al_2O_3) merely desorb. Therefore, a wave profile of the sensor response generally has one dynamic peak, which arises from flash catalytic combustion of target-gas molecules adsorbed over the sensor material film, and a subsequent static signal, which arises from general catalytic combustion of target-gas molecules at elevated temperatures, for the pulse heating of 0.4 s. The magnitude of gas response, ΔV_{MAX}, was defined as the difference between dynamic peak voltages in a target gas ($V_{MAX, g}$) and that in air ($V_{MAX, a}$).

3. Results and Discussions

3.1 Characterizations of Au/Pd nanoparticles and mp-Al_2O_3 powders

Figures 3 and 4 show a particle distribution and a TEM photograph of Au/Pd nanoparticles. The average particle size was about 6.0 nm from the TEM photograph, while the particle size measured by DLS was about 12.7 nm, probably because the Au/Pd nanoparticles were coated with a large number of polyethylene glycol monostearate molecules in the aqueous solution. Therefore, the particles size measured by DLS is considered to contain the size of these molecules. In addition, we confirmed that the ratio of Au to Pd (Au : Pd) in the Au/Pd nanoparticles was 23 : 77 in weight, by EDS equipped with TEM. This value measured by EDS was comparable to that in the precursor solution (Au : Pd = 20 : 80, composition ratio for preparation). Unfortunately, the core/shell structure of the nanoparticles was not confirmed by TEM. Therefore, the UV-VIS absorption spectrum of the Au/Pd nanoparticles was investigated, together with those of Au and Pd nanoparticles obtained by the same synthesis technique, as shown in Fig. 5. The Au nanoparticles showed a peak of plasmon absorption around 530 nm, whereas no plasmon adsorption of the Au/Pd nanoparticles as well as the Pd nanoparticles was

confirmed. Mizukoshi et al. reported that sonochemical reduction rate of Au(III) ions to Au was much larger than that of Pd(II) ion to Pd in the aqueous solution, and thus Au nanoparticles was firstly produced and Pd was subsequently coated around the Au nanoparticles in an aqueous solution containing $HAuCl_4$ and $PdCl_2$ by sonochemical reduction and the plasmon adsorption of Au nanoparticles drastically decreased with the coating of the Au nanoparticles with Pd [17]. Therefore, the no absorption peak around 530 nm of the Au/Pd nanoparticles strongly indicated that Au nanoparticles were mostly covered with Pd layer and thus the Pd layer only contributed to the light absorption and/or scattering. Based on these results from DLS, TEM, EDS and UV-VIS, it was confirmed that relatively uniform Au/Pd nanoparticles (diameter: ca. 6.0 nm) consisted of Au core (ca. 23 wt%) and Pd shell (ca. 77 wt%) were synthesized by sonochemical reduction technique in this study.

Figure S1 shows an XRD pattern and a TEM photograph of the mp-Al_2O_3 powder prepared, together with the particle-size distribution of the alumina nanoparticles observed in the TEM photograph. All peaks of the XRD pattern were assigned to γ-alumina (JCPDF No.: 10-0425), and the crystallite size (CS) calculated with both (400) and (440) peaks by using Scherrer equation (shape factor: 0.90) was ca. 4.1 nm. The TEM photograph shows that the most alumina nanoparticles were largely agglomerated to form secondary particles. The size of the alumina nanoparticles was distributed from 2 nm to 6.5 nm as shown in Fig. S1(b-i), and the mean diameter, which was calculated from several tens of the alumina nanoparticles confirmed in the TEM photograph, was ca. 4.4 nm. There results indicated that the most alumina nanoparticles was comprised of single crystals. The N_2 adsorption-desorption isotherms, pore-size distributions which were obtained by the BJH method, and the specific surface area (SSA), which was calculated by the BET method using the N_2 adsorption isotherm, of the mp-Al_2O_3 powder shown in Fig. S2. The mp-Al_2O_3 powder showed hysteresis behavior at higher relative pressures, which is associated with capillary condensation in mesopores [20]. The pore volume

of the mp-Al_2O_3 powder was relatively large, and the peak of pore distribution calculated from the adsorption isotherm (ca. 6.6 nm) was similar to that from the desorption isotherm (ca. 6.1 nm). These results indicated that the large amount of the well-developed and relatively-homogeneous mesopores was formed as meso-sized voids among alumina nanoparticles (mean diameter: 4.1 nm from XRD, 4.4 nm from TEM) in the secondary particles (agglomerates). In addition, the SSA of the mp-Al_2O_3 powder was ca. 239.6 m^2 g^{-1}. Assuming that the real density of γ-alumina is 3.5~4.0 g cm^{-3} [21] and the morphology of all the crystallites is spherical, the geometric surface area calculated from the CS of the mp-Al_2O_3 powder, 4.1 nm from XRD or 4.4 nm from TEM was ca. 366~418 m^2 g^{-1} or 341~389 m^2 g^{-1}, respectively. Considering the SSA of the mp-Al_2O_3 powder prepared (ca. 239.6 m^2 g^{-1}), all surface of the alumina nanoparticles does not contribute to the adsorption of N_2 molecules at 77 K, probably because the surface of crystallites was partially contacted each other.

Figure S3 shows variation in zeta potential of both the Au/Pd nanoparticles and the mp-Al_2O_3 powder with the magnitude of pH in water measured by ELS. The zeta potential of the mp-Al_2O_3 powder was almost zero at around pH 7, and the value positively shifted with a decrease in the pH and reached to ca. +28 mV at pH 4. On the other hand, the Au/Pd nanoparticles showed the negative zeta potential (< -10 mV) in the range of pH 3~7. Therefore, the pH of the aqueous solution containing the Au/Pd nanoparticle solutions was adjusted to ca. 4 after the mp-Al_2O_3 powder was added into the solution, to adsorb all the Au/Pd nanoparticles on the surface of the mp-Al_2O_3 powder effectively.

3.2 Characterizations of *n*(Au/Pd)/mp-Al_2O_3 and *n*(Au-Pd)/mp-Al_2O_3 powders

Figure 6 shows XRD patterns of representative samples (*1.0*(Au/Pd)/mp-Al_2O_3, *1.0*(Au-Pd)/mp-Al_2O_3 and *10*(Au-Pd)/mp-Al_2O_3 powders). XRD patterns of both the *1.0*(Au/Pd)/mp-Al_2O_3 and *1.0*(Au-Pd)/mp-Al_2O_3 powders were assigned only to γ-alumina (CS: ca. 3.8 nm for

1.0(Au/Pd)/mp-Al_2O_3, ca. 3.9 nm for *1.0*(Au-Pd)/mp-Al_2O_3) and the pH adjustment for the Au/Pd loading as well as the heat treatment in H_2 at 350°C for Au-Pd loading had little effect on the increase in their CS values. On the other hand, the large loading amount of Au and Pd (10 wt%) onto the mp-Al_2O_3 powder by an impregnation method showed large XRD peaks of both Au and Pd, together with that of γ-alumina. The CS value of the γ-alumina cannot be calculated due to the existence of the large Au and Pd peaks. However, the CS values of Au and Pd nanoparticles calculated from their (111) peak were ca. 22.0 nm and ca. 8.6 nm, respectively. Figure S5 shows N_2 adsorption-desorption isotherms and pore-size distributions of the *1.0*(Au/Pd)/mp-Al_2O_3, *1.0*(Au-Pd)/mp-Al_2O_3 and *10*(Au-Pd)/mp-Al_2O_3 powders together with their SSA, and Fig. 6 shows variation in SSA of all *n*(Au/Pd)/mp-Al_2O_3 and *n*(Au-Pd)/mp-Al_2O_3 powders with the amount of noble metal (Au + Pd) loaded. The loading of Au/Pd or Au-Pd onto the mp-Al_2O_3 powder increased the volume of pores with a diameter of less than ca. 4 nm (Figs. S5(a) and (b)), and the SSA of the *1.0*(Au/Pd)/mp-Al_2O_3 and *1.0*(Au-Pd)/mp-Al_2O_3 powders was slightly larger than that of the mp-Al_2O_3 powder. The small amount of Au/Pd or Au-Pd loading (less than 1 wt%) onto the mp-Al_2O_3 powder tended to increase the SSA, as shown in Fig. 6. In addition, the distributions of pores with a diameter of more than ca. 4 nm as well as N_2 adsorption-desorption isotherms of the *1.0*(Au/Pd)/mp-Al_2O_3 and *1.0*(Au-Pd)/mp-Al_2O_3 powders were not much different than those of the mp-Al_2O_3 powder (see Fig. S2). However, the large amount of Au-Pd loading (10 wt%) onto the mp-Al_2O_3 powder increased the volume of pores with a diameter of less than ca. 4 nm and slightly narrowed the pore-size distribution around 6~7 nm in diameter (Fig. S5(b)(iii)), and the SSA of the *10*(Au-Pd)/mp-Al_2O_3 powder was comparable to that of the mp-Al_2O_3 powder (Fig. 6). Anyhow, these results indicated that the loading of Au/Pd or Au-Pd had less influence on the mesostructure of the mp-Al_2O_3 powder.

In order to investigate the compositional and microstructural differences between Au/Pd and

Au-Pd loaded on the surface of the mp-Al_2O_3 powder, the morphology of the representative samples, *1.0*(Au/Pd)/mp-Al_2O_3 and *1.0*(Au-Pd)/mp-Al_2O_3 powders, was characterized by TEM and EDS, as shown in Fig. 7(a) and Fig. 7(b), respectively. Some of their Au/Pd and Au-Pd nanoparticles were marked by arrowheads. Even though both the powders showed almost the same pore-size distribution and SSA, there are much morphological differences between them. The Au/Pd nanoparticles were relative homogeneously loaded on the surface of the mp-Al_2O_3 powder, and the ratio of Au to Pd (Au : Pd) in the Au/Pd nanoparticles at the whole region in Fig. 7(a)(i) was 24 : 76 in weight, which was quite comparable to that in Au/Pd nanoparticles in Fig. 4 (23 : 77). The average diameter of Au/Pd nanoparticles loaded was ca. 5.9 nm, which is calculated from all Au/Pd nanoparticles in Fig. 7(a)(ii), and the ratio of Au to Pd in regions enclosed by two circles was 29 : 71 and 25 : 75 in weight. These results indicate that the Au/Pd nanoparticles were loaded on the mp-Al_2O_3 surface without any large compositional and morphological changes. In addition, the morphology of the alumina nanoparticles of the *1.0*(Au/Pd)/mp-Al_2O_3 powder also seems to remain unaffected by the loading of Au/Pd nanoparticles in the colloidal aqueous solution (cf. Fig. S1(b)). The homogeneous and highly dispersible loading of the Au/Pd nanoparticles on the surface of the mp-Al_2O_3 powder must result from the optimal pH control of the colloidal solution containing the Au/Pd nanoparticles and the mp-Al_2O_3 powders in order to control surface electric charge of both the Au/Pd nanoparticles (negative charge) and the mp-Al_2O_3 powders (positive charge). On the other hand, the average diameter of noble-metal nanoparticles in the *1.0*(Pd-Au)/mp-Al_2O_3 powders, which were marked by white arrowheads in Fig. 7(b) was ca. 8.1 nm, and the size was a little bit larger than that of Au/Pd nanoparticles of the *1.0*(Au/Pd)/mp-Al_2O_3 powder and comparable to the CS value of Pd of the *10*(Au-Pd)/mp-Al_2O_3 powder (ca. 8.6 nm), which was calculated from Fig. S4(c). The ratio of Au to Pd in the region enclosed by the circle was 4 : 96 in weight. In addition, a little amount of large particles with a diameter of several tens of nanometers (diameter of one

marked by the black arrowhead: ca. 70 nm) were also observed as shown in Fig. 7(b), and the ratio of Au to Pd was 92 : 8[*] in weight. These results showed that the large amount of Au components formed the large particles and the most Pd-rich components mildly agglomerated as a little large Pd-based nanoparticles during the impregnation and subsequent H_2 treatment at 350°C, in comparison with Au/Pd nanoparticles of the *1.0*(Au/Pd)/mp-Al_2O_3 powder.

Adsorption/combustion-type gas sensors were actually fired at 700°C for 2 h in air, before the measurements of their gas-sensing properties, to improve the thermal stability. Therefore, representative two powders, *1.0*(Au/Pd)/mp-Al_2O_3 and *1.0*(Au-Pd)/mp-Al_2O_3 powders, were heat-treated at 700°C for 2 h in air, and then characterized by N_2 adsorption-desorption and TEM. Figure S6 shows N_2 adsorption-desorption isotherms, pore-size distributions, and SSA of the two powders. The heat treatment at 700°C shifted the hysteresis loops to higher relative pressures, and thus slightly enlarged the pore size, for both the samples. In addition, the heat treatment reduced not only the volume of pores with a diameter of less than ca. 4 nm but also the SSA values, and thus both the values of *1.0*(Au/Pd)/mp-Al_2O_3 and *1.0*(Au-Pd)/mp-Al_2O_3 powders were comparable to those of mp-Al_2O_3 powder (see Fig. S2). Figure 8 shows TEM photographs of the *1.0*(Au/Pd)/mp-Al_2O_3 and *1.0*(Au-Pd)/mp-Al_2O_3 powders heat-treated at 700°C for 2 h in air, with the ratio of Au to Pd in some regions. The core/shell structure of Au/Pd nanoparticles on the surface of the heat-treated *1.0*(Au/Pd)/mp-Al_2O_3 powder were entirely destroyed during the heat treatment, and the ratio of Au to Pd became extremely heterogeneous as shown in Fig. 8(a), compared with the as-prepared one (Fig. 7(a)). Namely, the Pd content (Pd/(Pd+Au), 0.87~0.90 in weight) at the regions formed with nanoparticles observed in the relatively light color (regions B, D, and F) of the heat-treated *1.0*(Au/Pd)/mp-Al_2O_3 powder was slightly larger than that on the surface of the as-prepared *1.0*(Au/Pd)/mp-

[*] This ratio contains a given amount of Au and Pd components existing and/or attaching around the large particle marked by the black arrowhead.

Al_2O_3 powder, and the size of the Pd-rich nanoparticles could not be clearly confirmed in these TEM photographs, probably because of the extremely-high dispersibility of Pd on the alumina nanoparticles after the destruction of the core/shell structure. The Pd content drastically decreased as the color in the photographs became dark (regions A, C, and E), and many large Au-based particles with a diameter of 20~25 nm (Au : Pd[†] (typically measured) = 65 : 35, 57 : 43, and 52 : 48 in weight) were observed on the surface of the heat-treated *1.0*(Au/Pd)/mp-Al_2O_3 powder. This morphology indicates that the Au components drastically migrate on the alumina surface and they sintered to each other at 700°C. However, the size of the large Au-based particles was much smaller than that of the as-prepared *1.0*(Au-Pd)/mp-Al_2O_3 powder (see Fig. 7(b)). On the other hand, surface morphology of the heat-treated *1.0*(Au-Pd)/mp-Al_2O_3 powder was comparable to that of the as-prepared *1.0*(Au-Pd)/mp-Al_2O_3 powder. However, the size of the large Au-based particles (80~100 nm in diameter) increased, and the Pd content of the Pd-rich region (0.97~0.98) slightly increased after the heat treatment, because of the further agglomeration of the Au component to the large particles. In addition, the size of Pd-based nanoparticles (ca. 5~15 nm in diameter) was relatively heterogeneous and slightly increased by the heat treatment.

3.3 Gas-sensing properties of *n*(Au/Pd)/mp-Al_2O_3 and *n*(Au-Pd)/mp-Al_2O_3 sensors

Figure 9 shows the sensor-signal profiles of *1.0*(Au/Pd)/mp-Al_2O_3 and *1.0*(Au-Pd)/mp-Al_2O_3 sensors to 1000 ppm ethanol in air at the pulse-heating temperature of 250~450°C, together with those of a *10*(Au-Pd)/mp-Al_2O_3 sensor, which showed the largest ethanol-sensing properties in the previous study [16]. When these sensors were pulse-heated to 450°C, the *10*(Au-Pd)/mp-Al_2O_3 sensor showed the largest ΔV_{MAX} to ethanol among them, and the

[†] This ratio contains a given amount of Au and Pd components existing and/or attaching around the large particle marked by the black arrowhead.

response speed of the *10*(Au-Pd)/mp-Al_2O_3 sensor was much faster than those of other sensors, because the large amount of Au and Pd (*n*: *10* wt%) loaded on mp-Al_2O_3 effectively burned ethanol molecules adsorbed on the surface. In addition, the ΔV_{MAX} and the response speed of the *1.0*(Au/Pd)/mp-Al_2O_3 sensor were comparable to those of the *1.0*(Au-Pd)/mp-Al_2O_3 sensor. However, the ΔV_{MAX} of the *n*(Au-Pd)/mp-Al_2O_3 sensors (*n = 1.0* and *10*) drastically decreased with a decrease in the pulse-heating temperatures, while the *1.0*(Au/Pd)/mp-Al_2O_3 sensor showed the large ethanol response even at 350°C, which was comparable to that at 450°C, and thus the ΔV_{MAX} of the *1.0*(Au/Pd)/mp-Al_2O_3 sensor was much larger than those of the *n*(Au-Pd)/mp-Al_2O_3 sensors (*n = 1.0* and *10*) at 350°C, irrespective of the relatively slow response speed in comparison with that of the *10*(Au/Pd)/mp-Al_2O_3 sensor. On the other hand, the ΔV_{MAX} of all the sensors was extremely low at the pulse-heating temperature of 250°C, but only the *1.0*(Au/Pd)/mp-Al_2O_3 sensor showed relatively large response enough to detect 1000 ppm ethanol. Figure 10 shows the sensor-signal profiles of *n*(Au/Pd)/mp-Al_2O_3 and *n*(Au-Pd)/mp-Al_2O_3 sensors (*n = 0.1* and *0.5*) to 1000 ppm ethanol in air at the pulse-heating temperatures of 250~450°C. As the amount of Au and Pd loaded (*n*) decreased, the ΔV_{MAX} to ethanol of both the *n*(Au/Pd)/mp-Al_2O_3 and *n*(Au-Pd)/mp-Al_2O_3 sensors gradually decreased at all the pulse-heating temperatures and the difference in the ΔV_{MAX} between *n*(Au/Pd)/mp-Al_2O_3 and *n*(Au-Pd)/mp-Al_2O_3 sensors expanded, especially at 450°C. These dependences of the ethanol-sensing properties on both the amount of Au and Pd loaded (*n*) and pulse-heating temperature between *n*(Au/Pd)/mp-Al_2O_3 and *n*(Au-Pd)/mp-Al_2O_3 sensors may originate from the loading state of Au and Pd on the alumina surface, considering the surface morphology of the heat-treated *1.0*(Au/Pd)/mp-Al_2O_3 and *1.0*(Au-Pd)/mp-Al_2O_3 powders (see Fig. 8). The Pd-based nanoparticles of the *n*(Au/Pd)/mp-Al_2O_3 powder were highly dispersed on the alumina nanoparticles in comparison with those of the *n*(Au-Pd)/mp-Al_2O_3 powder, and the Au content of the *n*(Au/Pd)/mp-Al_2O_3 powder at the surface regions containing many Pd-based

nanoparticles (Au/(Pd+Au), 0.10~0.13 in weight) was larger than that of the *1.0*(Au-Pd)/mp-Al_2O_3 powder (0.02~0.03 in weight). These structural and/or compositional characteristics may be effective in improving the flash catalytic combustion property of ethanol absorbed and/or enhancing the amount of ethanol absorbed on the mp-Al_2O_3 powder. In addition, thermal conductivity of the sensing materials is one of important factors to control gas-sensing properties of adsorption/combustion-type gas sensors [12, 16]. The size of large Au-based particles of the *1.0*(Au/Pd)/mp-Al_2O_3 powder (20~25 nm in diameter) was smaller than that of the *1.0*(Au-Pd)/mp-Al_2O_3 (80~100 nm in diameter), and then the large Au-based particles of the *1.0*(Au/Pd)/mp-Al_2O_3 powder highly dispersed in comparison with those of the *1.0*(Au-Pd)/mp-Al_2O_3. This highly-dispersive loading of the large Au-based particles may enhance the thermal conductivity of the *n*(Au/Pd)/mp-Al_2O_3, and thus improve the ethanol-sensing properties.

Figure 11 shows the sensor-signal profiles to 1000 ppm toluene and *n*-hexane of *0.5*(Au/Pd)/mp-Al_2O_3 and *0.5*(Au-Pd)/mp-Al_2O_3 sensors as a representative in air at the pulse-heating temperature of 250~450°C, and Fig. 12 summarizes the variations in the ΔV_{MAX} to 1000 ppm toluene and *n*-hexane in air with the amount of Au and Pd loaded (*n*) of *n*(Au/Pd)/mp-Al_2O_3 and *n*(Au-Pd)/mp-Al_2O_3 sensors, together with those to 1000 ppm ethanol. The ΔV_{MAX} to toluene of the *n*(Au/Pd)/mp-Al_2O_3 sensors was larger than that of the *n*(Au-Pd)/mp-Al_2O_3 sensors, and the ΔV_{MAX} to toluene of both the series of sensors was also relatively dependent on the pulse-heating temperature as well as the amount of Au and Pd loaded (*n*), such as their ΔV_{MAX} to ethanol. However, the ΔV_{MAX} to toluene was much smaller than that to ethanol, but it was much larger than that to *n*-hexane, for all sensors. In addition, the ΔV_{MAX} to *n*-hexane of the *n*(Au/Pd)/mp-Al_2O_3 sensors was comparable to that of the *n*(Au-Pd)/mp-Al_2O_3 sensors, and the ΔV_{MAX} to *n*-hexane of both the sensors were not much dependent on both the pulse-heating temperatures as well as the amount of Au and Pd loaded (*n*). Interestingly, in addition, the shape

of some sensor-signals of the *n*(Au/Pd)/mp-Al_2O_3 sensors, especially that of the dynamic output by flash combustion, depended upon the kind of target gases, especially at the pulse-heating temperature of 450°C [11]. For example, the *0.5*(Au/Pd)/mp-Al_2O_3 sensor showed the relatively broad sensor-signal profile to ethanol (see Fig. 10(a)(iii)), while the signal profile to toluene was much sharper than that to ethanol, and the signal profile to *n*-hexane was a little erratic in comparison with those of other target gases, as shown in Fig. 11(a)(iii) and (b)(iii). Their detail analyses may provide the fundamentals for the selective detection of these gases. These sensing properties dependent on the kinds of target gases seem to be greatly affected by polar characteristics of target gases, dipole moment (ethanol: 1.69 D, toluene: 0.36 D, *n*-hexane: 0 D) and dielectric constant (ethanol: 24.6, toluene: 2.38, *n*-hexane: 1.88). Namely, the ΔV_{MAX} of all sensors to ethanol, toluene and *n*-hexane increased with an increase in their dipole moment and the dielectric constant, probably because the target-gas molecules with larger dipole moment and/or dielectric constant were easily adsorbed on the alumina surface. Therefore, we realized that the increase in the adsorbed amount of target-gas molecules as well as the improvements in the catalytic combustion properties of target-gas molecules and the thermal conductivity, were quite important for the enhancement of the gas-sensing properties of adsorption/combustion-type gas sensors.

Figure 13(a) shows the representative sensor-signal profiles of the *0.5*(Au/Pd)/mp-Al_2O_3 sensor to 10~1000 ppm ethanol, toluene and *n*-hexane in air at the pulse-heating temperature of 450°C. The ΔV_{MAX} values in the sensor-signal profiles to three target gases of the *0.5*(Au/Pd)/mp-Al_2O_3 sensor decreased and the shape of dynamic output broadened with a decrease in the concentration, but the sensor surely detected 10 ppm target gases (ca. 35 mV for ethanol, ca. 22 mV for toluene, and ca. 11 mV for *n*-hexane) and thus it is expected that the concentration threshold to detect these gases is much low. Variations in logarithmic ΔV_{MAX} to ethanol, toluene and *n*-hexane of *0.5*(Au/Pd)/mp-Al_2O_3 and *0.5*(Au-Pd)/mp-Al_2O_3 sensors with

concentration of the three target gases in air at the pulse-heating temperature of 450°C are shown in Fig. 13(b). The sensitivity (the slope of the relationship between log (ΔV_{MAX}) and log (concentration)) to ethanol was comparable to that to toluene, and these sensitivity was much larger than that to *n*-hexane, as for the *0.5*(Au/Pd)/mp-Al_2O_3 sensor. On the other hand, apparent sensitivity to ethanol and *n*-hexane of the *0.5*(Au-Pd)/mp-Al_2O_3 sensor was larger than that of the *0.5*(Au/Pd)/mp-Al_2O_3 sensor, but the concentration threshold seems to be very low (ΔV_{MAX} to 10 ppm ethanol and *n*-hexane: only ca. 9.7 mV and ca. 7.6 mV, respectively). In addition, toluene sensitivity of the *0.5*(Au/Pd)/mp-Al_2O_3 sensor was very small. These results indicated that the *0.5*(Au/Pd)/mp-Al_2O_3 sensor showed excellent sensitivity as well as large response to these target gases, in comparison with those of the *0.5*(Au-Pd)/mp-Al_2O_3 sensor.

4. Conclusions

Synthesis of uniform core(Au)/shell(Pd) nanoparticles (Au : Pd = 1 : 4 in weight, particles size: ca. 6.0 nm) by sonochemical reduction succeeded, and the Au/Pd nanoparticles obtained were high-dispersively loaded onto the surface of the mp-Al_2O_3 powder (SSA: ca. 239.6 $m^2 g^{-1}$), which were prepared by a solvothermal method. The pore-size distributions and the SSA value of *n*(Au/Pd)/mp-Al_2O_3 powders, especially which were heat-treated at 700°C were roughly comparable to those of the unloaded mp-Al_2O_3 powder and *n*(Au-Pd)/mp-Al_2O_3 powders prepared by general impregnation technique. The sensing properties to ethanol, toluene and *n*-hexane of *n*(Au/Pd)/mp-Al_2O_3 sensors were larger than those of *n*(Au-Pd)/mp-Al_2O_3 sensors, especially at a smaller amount of Au and Pd loaded as well as at lower operating temperatures, probably because the highly dispersed Pd-based nanoparticles and relatively large Au-based particles on the alumina nanoparticles, which remained on the alumina surface after the destruction of the core/shell structure by heat treatment at 700°C, improved the catalytic combustion properties of these gases and the thermal conductivity, respectively. In addition, the

n(Au/Pd)/mp-Al_2O_3 sensors showed much larger response to ethanol than those to toluene and *n*-hexane, probably because of the difference in the magnitude of polarity (dipole moment and dielectric constant) of their molecules, but the sensors obviously detected even 10 ppm *n*-hexane with the extremely low dipole moment and dielectric constant.

References

1. B. Guieysse, C. Hort, V. Platel, R. Munoz, M. Ondarts, S. Revah, Biological treatment of indoor air for VOC removal: Potential and challenges, Biotechnol. Adv. 26 (2008) 398–410.
2. T. Petry, D. Vitale, F. J. Joachim, B. Smith, L. Cruse, R. Mascarenhas, S. Schneider, M. Singal, Human health risk evaluation of selected VOC, SVOC and particulate emissions from scented candles, Regul. Toxicol. Pharmacol., in press.
3. S. Herberger, M. Herold, H. Ulmer, A. Burdack-Freitag, F. Mayer, Detection of human effluents by a MOS gas sensor in correlation to VOC quantification by GC/MS, Building and Environment 45 (2010) 2430–2439.
4. R.-S. Jian, L.-Y. Sung, C.-J. Lu, Measuring real-time concentration trends of individual VOC in an elementary school using a sub-ppb detection μGC and a single GC–MS analysis, Chemosphere 99 (2014) 261–266.
5. C. Tasaltin, F. Basarir, Preparation of flexible VOC sensor based on carbon nanotubes and gold nanoparticles, Sens. Actuators B 194 (2014) 173-179.
6. S. Stegmeier, M. Fleischer, P. Hauptmann, Influence of the morphology of platinum combined with β-Ga_2O_3 on the VOC response of work function type sensors, Sens. Actuators B 148 (2010) 439-449.
7. M. Mori, H. Nishimura, Y. Itagaki, Y. Sadaoka, Potentiometric VOC detection in air using 8YSZ-based oxygen sensor modified with $SmFeO_3$ catalytic layer, Sens. Actuators B 142

(2009) 141-146.

8. I. Elmi, S. Zampolli, E. Cozzani, F. Mancarella, G.C. Cardinali, Development of ultra-low-power consumption MOX sensors with ppb-level VOC detection capabilities for emerging applications, Sens. Actuators B 135 (2008) 342-351.
9. M. Suresh, N. J. Vasa, V. Agarwal, J. Chandapillai, UV photo-ionization based asymmetric field differential ion mobility sensor for trace gas detection, Sens. Actuators B 195 (2014) 44-51.
10. S. Panigrahi, S. Sankaran, S. Mallik, B. Gaddam, A. A. Hanson, Olfactory receptor-based polypeptide sensor for acetic acid VOC detection, Mater. Sci. Eng. C 32 (2012) 1307-1313.
11. T. Sasahara, A. Kido, T. Sunayama, S. Uematsu, M. Egashira, Identification and quantification of alcohol by a micro gas sensor based on adsorption and combustion, Sens. Actuators B 99 (2004) 532-538.
12. T. Sasahara, A. Kido, H. Ishihara, T. Sunayama, M. Egashira, Highly sensitive detection of volatile organic compounds by an adsorption/combustion-type sensor based on mesoporous silica, Sens. Actuators B 108 (2005) 478-483.
13. T. Sasahara, H. Kato, A. Saito, M. Nishimura, M. Egashira, Development of a ppb-level sensor based on catalytic combustion for total volatile organic compounds in indoor air, Sens. Actuators B 126 (2007) 536-543.
14. H. Shibata, T. Hyodo, T. Sasahara, Y. Shimizu, M. Egashira, Adsorption and combustion behavior of organic compounds on sensor materials used for adsorption/combustion-type sensors, Chemical Sensors 21 (2005) 139-141.
15. T. Hyodo, K. Hieda, T. Sasahara, Y. Shimizu, M. Egashira, Design of catalyst materials for adsorption/combustion-type gas sensors, Chemical Sensors 24 (2008) 67-69.
16. Y. Yuzuriha, T. Hyodo, T. Sasahara, Y. Shimizu, M. Egashira, Mesoporous Al_2O_3 co-Loaded with Pd and Au as a combustion catalyst for adsorption/combustion-type gas

sensors, Sensor Lett. 9 (2011) 409-413.

17. Y. Muzukoshi, K. Okitsu, Y. Maeda, Y. A. Yamamoto, R. Oshima, Y. Nagata, Sonochemical preparation of bimetallic nanoparticles of gold/palladium in aqueous solution, J. Phys. Chem. B, 101 (1997) 7033-7037.
18. K. Okitsu and M. Murakami, S. Tanabe, H. Matsumoto, Sonochemical preparation and catalytic behavior of highly dispersed palladium nanoparticles on alumina, Chem. Lett. (2000) 1336-1337.
19. T. Nakagawa, H. Nitani, S. Tanabe, K. Okitsu, S. Seino, Y. Mizukoshi, T. A. Yamamoto, Structural analysis of Au/Pd nanoparticles dispersed in porous silica matrix by TEM, XRD and XAFS, Ultrasonics Sonochemistry, 12 (2005) 249-254.
20. K. S. W. Sing, Reporting Physisorption data for gas/solid systems with special reference to the determination of surface area and porosity, Pure & Appl. Chem. 54 (1982) 2201-2218.
21. US Research Nanomaterials, Material Safety Data Sheet (MSDS) for Stock No. US3007, US3023 and US3024 (2013), Sigma-Aldrich, MSDS for Product No. 544833 and 517747 (2012), and Wako Pure Chemical, MSDS No. JW010152 and JW010829 (2009).

Figure Captions

Fig. 1. (a) Schematic drawing of an adsorption/combustion-type gas sensor and (b) a bridge circuit containing the micro-sensor chip.

Fig. 2. Typical sensor-signal profile of adsorption/combustion-type gas sensors. ΔV (vertical axis): the difference between output voltage in a target gas (V_g) and that in air (V_a).

Fig. 3. Particle-size distribution of Au/Pd nanoparticles synthesized in this study.

Fig. 4. TEM photograph of Au/Pd nanoparticles synthesized in this study.

Fig. 5. UV-VIS absorption spectrum of Au/Pd nanoparticles synthesized in this study.

Fig. 6. Variation in SSA of all *n*(Au-Pd)/mp-Al_2O_3 and *n*(Au-Pd)/mp-Al_2O_3 powders prepared in this study, with the amount of noble metal (Au + Pd) loaded.

Fig. 7. TEM photographs of *1.0*(Au/Pd)/mp-Al_2O_3 and *1.0*(Au-Pd)/mp-Al_2O_3 powders, together with the ratio of Au to Pd (Au : Pd) of some regions in weight.

Fig. 8. TEM photographs of *1.0*(Au/Pd)/mp-Al_2O_3 and *1.0*(Au-Pd)/mp-Al_2O_3 powders heat-treated at 700°C for 2 h in air, together with the ratio of Au to Pd (Au : Pd) of some regions in weight.

Fig. 9. Sensor-signal profiles of *1.0*(Au/Pd)/mp-Al_2O_3 and *1.0*(Au-Pd)/mp-Al_2O_3 sensors to 1000 ppm ethanol in air at the pulse-heating temperature of 250~450°C, together with those of a *10*(Au-Pd)/mp-Al_2O_3 sensor.

Fig. 10. Sensor-signal profiles of *n*(Au/Pd)/mp-Al_2O_3 and *n*(Au-Pd)/mp-Al_2O_3 sensors (*n* = *0.1* and *0.5*) to 1000 ppm ethanol in air at the pulse-heating temperatures of 250~450°C.

Fig. 11. Sensor-signal profiles to 1000 ppm toluene and *n*-hexane of *0.5*(Au/Pd)/mp-Al_2O_3 and *0.5*(Au-Pd)/mp-Al_2O_3 sensors in air at the pulse-heating temperature of 250~450°C.

Fig. 12. Variations in the ΔV_{MAX} to 1000 ppm ethanol, toluene and *n*-hexane in air with the

amount of Au and Pd loaded (*n*) of *n*(Au/Pd)/mp-Al_2O_3 and *n*(Au-Pd)/mp-Al_2O_3 sensors.

Fig. 13. (a) Sensor-signal profiles of the *0.5*(Au/Pd)/mp-Al_2O_3 sensor to 10, 100 and 1000 ppm ethanol, toluene and *n*-hexane and (b) dependence of logarithmic ΔV_{MAX} of *0.5*(Au/Pd)/mp-Al_2O_3 and *0.5*(Au-Pd)/mp-Al_2O_3 sensors on concentration of ethanol, toluene and *n*-hexane in air at the pulse-heating temperature of 450°C.

(a) Schematic drawing of a sensor

(i) Cross-sectional view

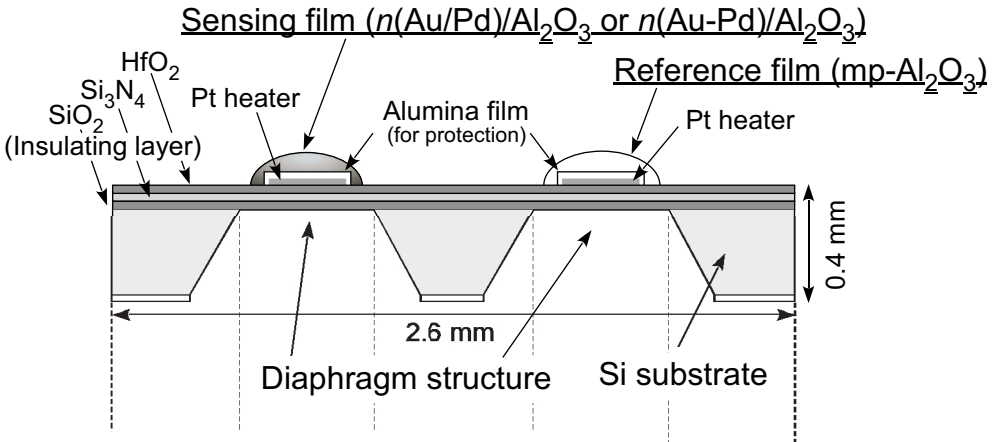

(ii) Top view

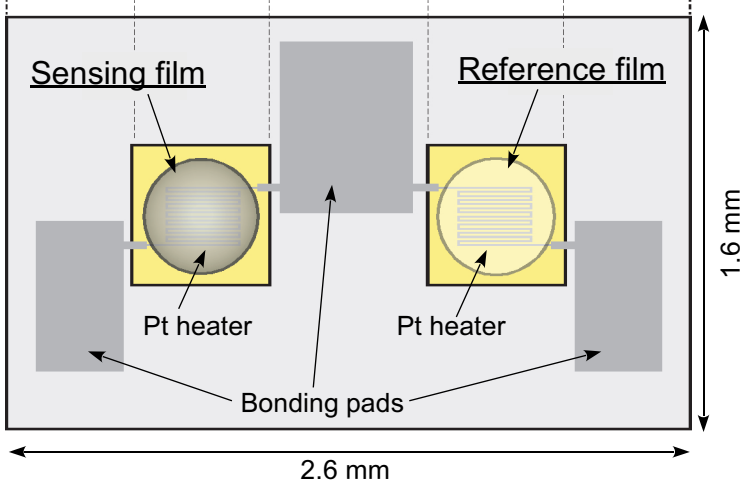

(b) Measurement circuit

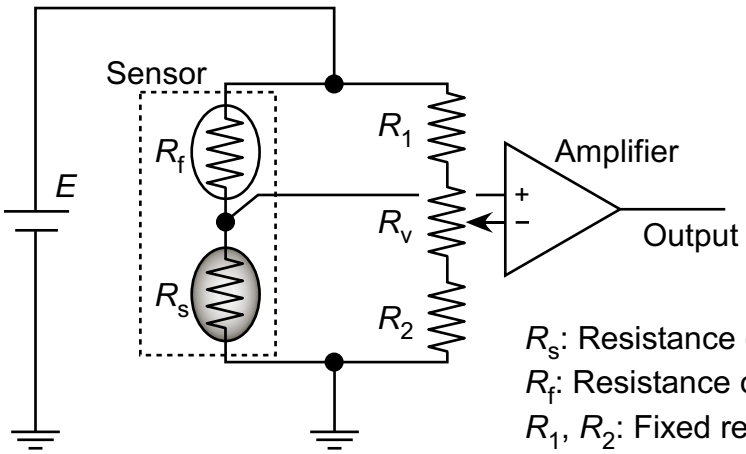

R_s: Resistance of a sensing film
R_f: Resistance of a reference film
R_1, R_2: Fixed resistances
R_v: Variable resistance
E: Bridge voltage

Fig. 1. Hyodo et al.

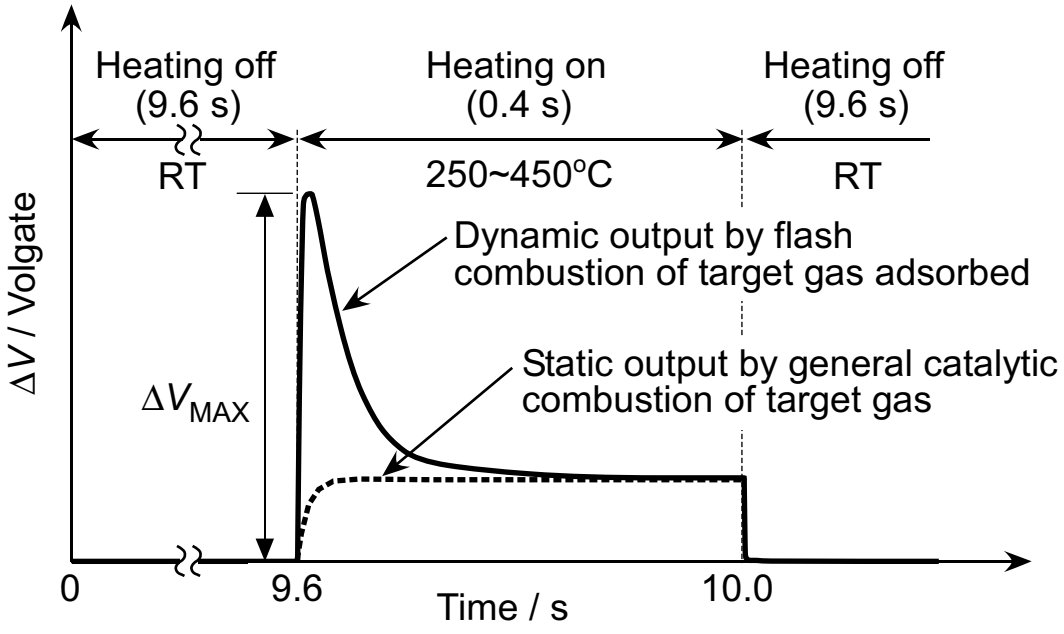

Fig. 2. Hyodo et al.

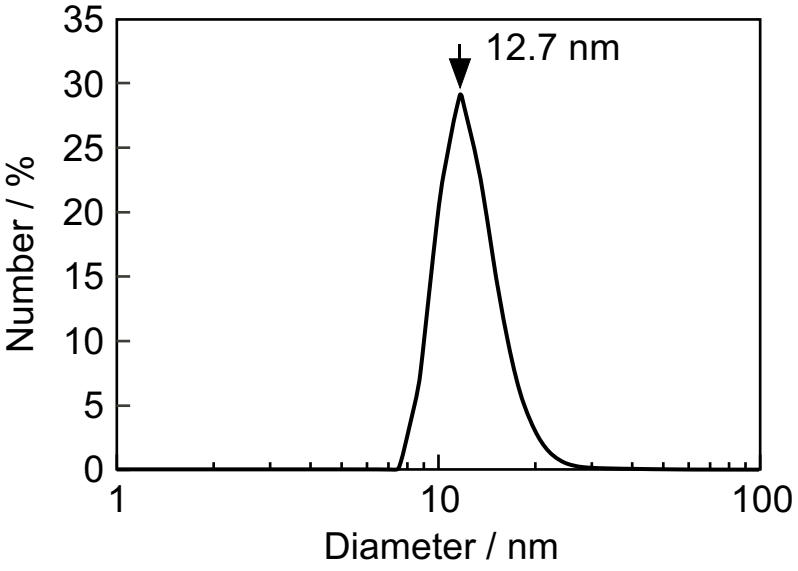

Fig. 3. Hyodo et al.

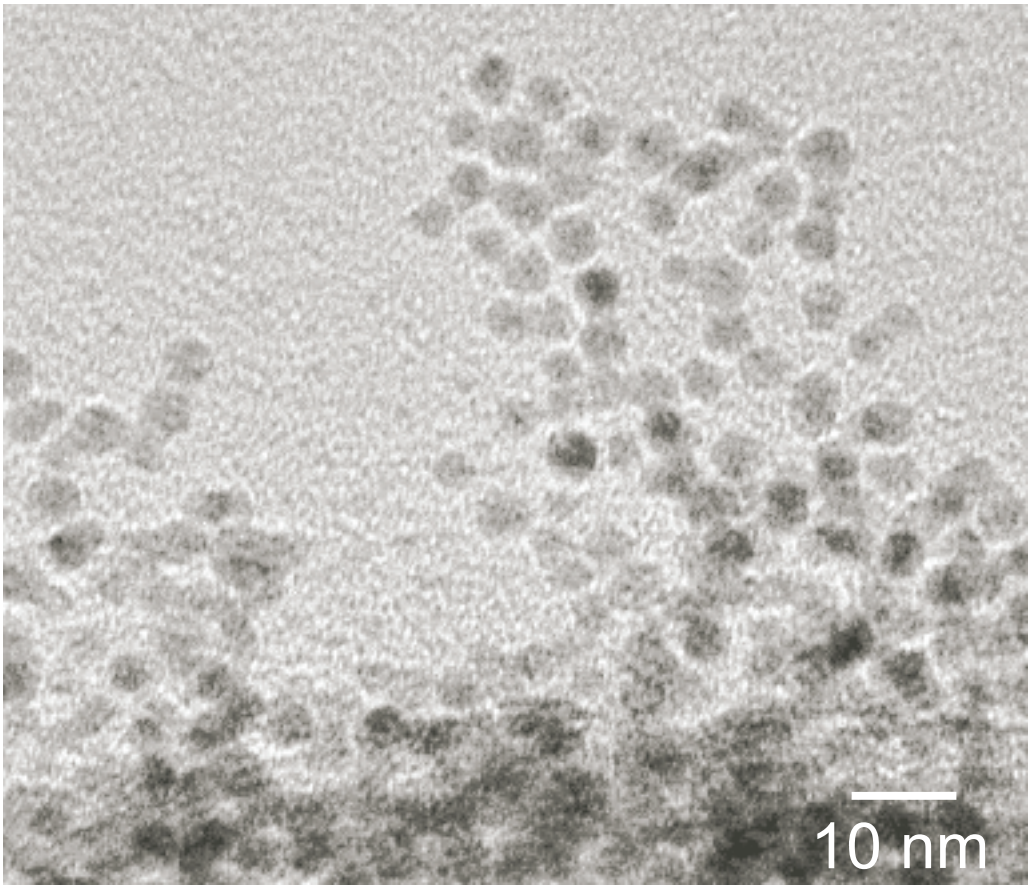

Fig. 4. Hyodo et al.

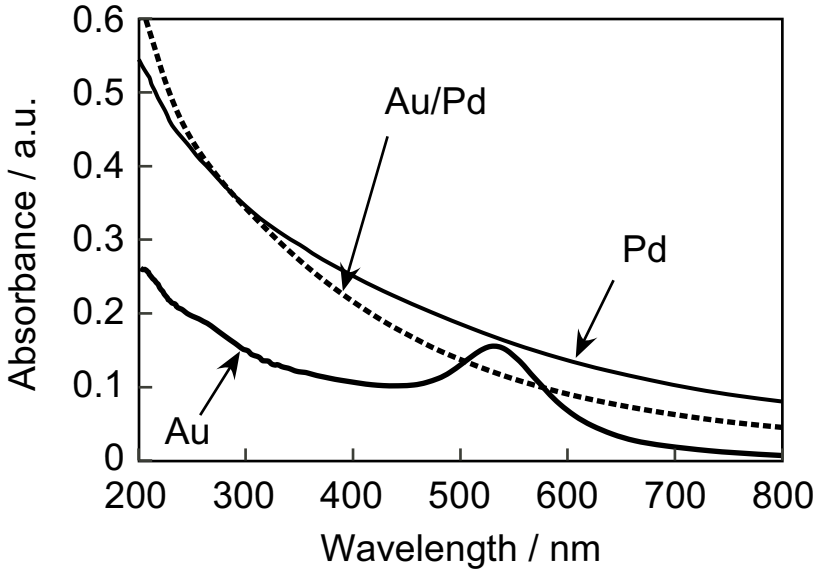

Fig. 5. Hyodo et al.

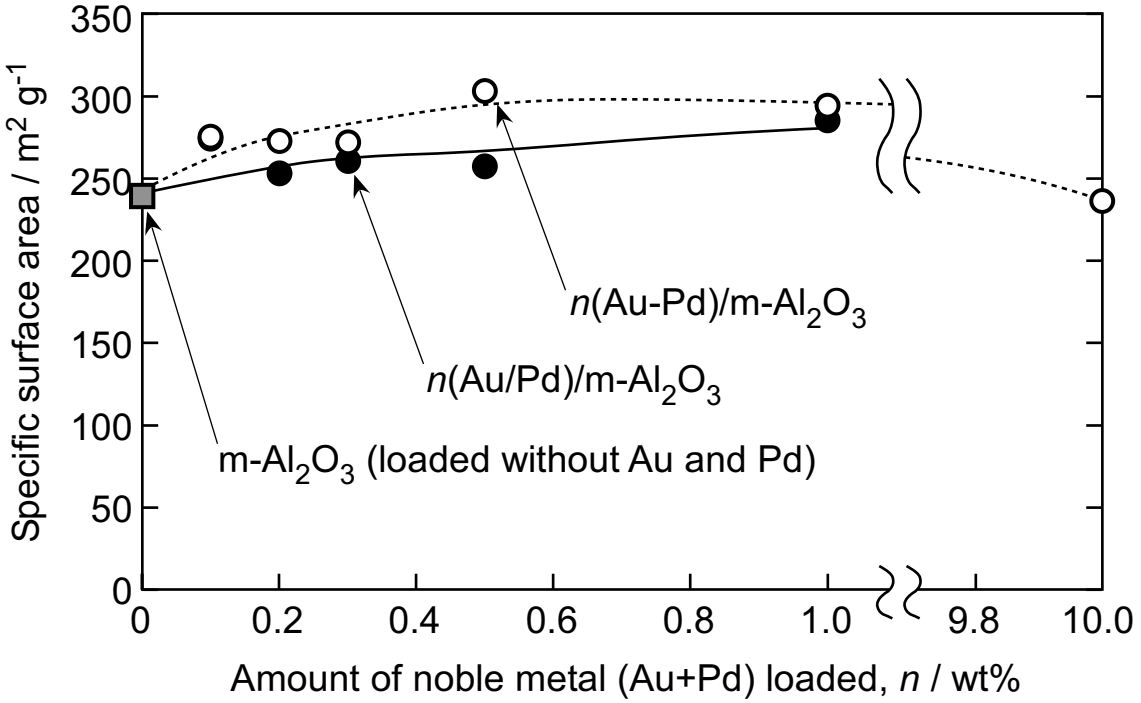

Fig. 6. Hyodo et al.

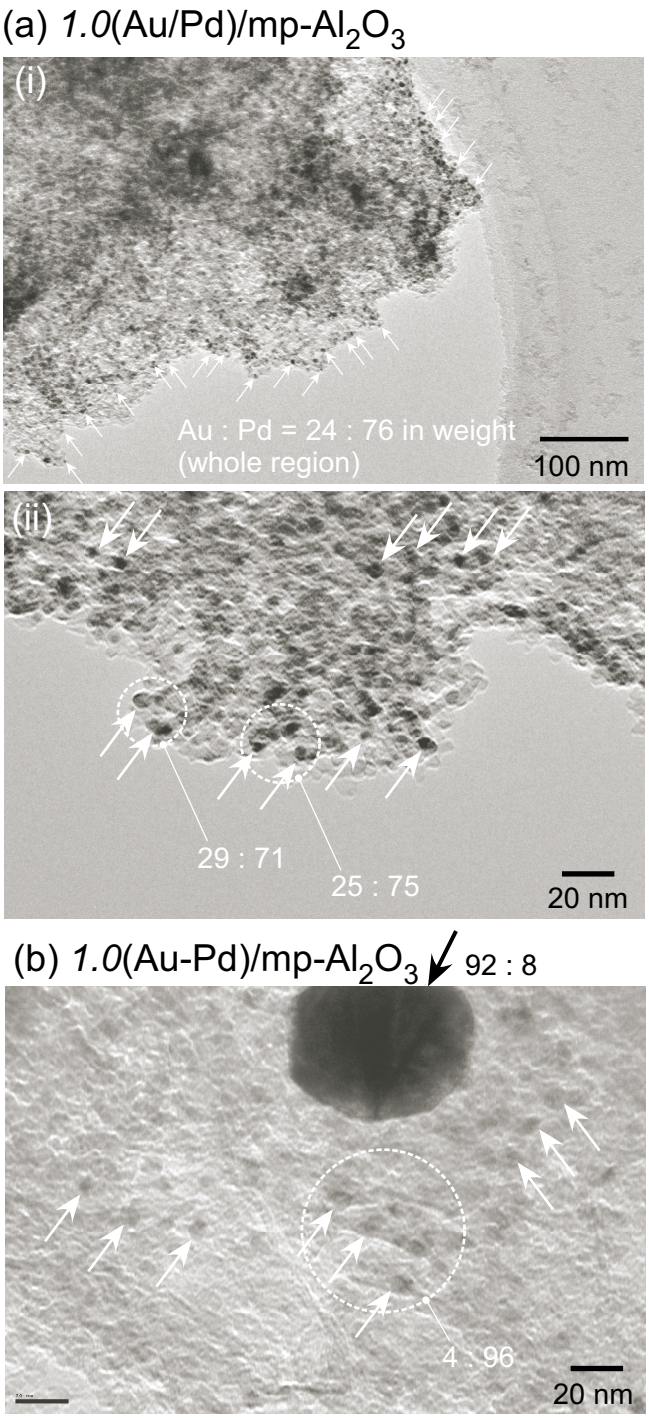

Fig. 7. Hyodo et al.

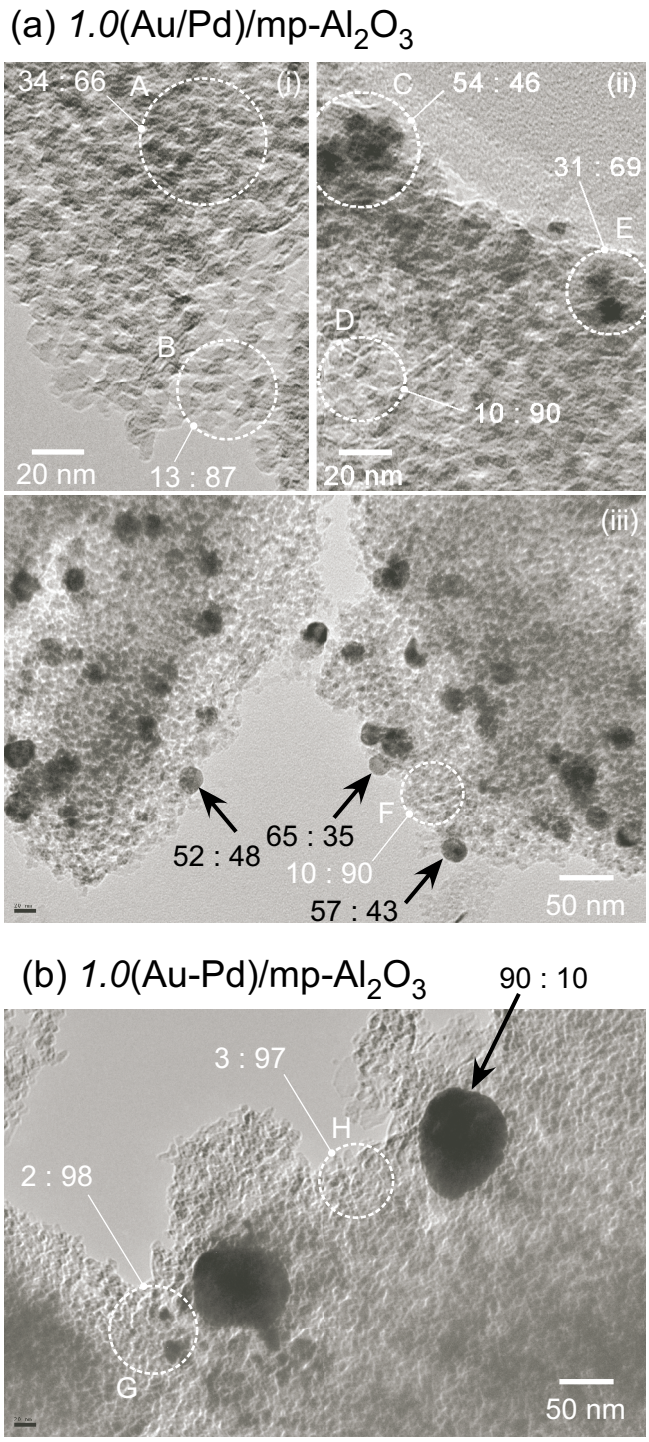

Fig. 8. Hyodo et al.

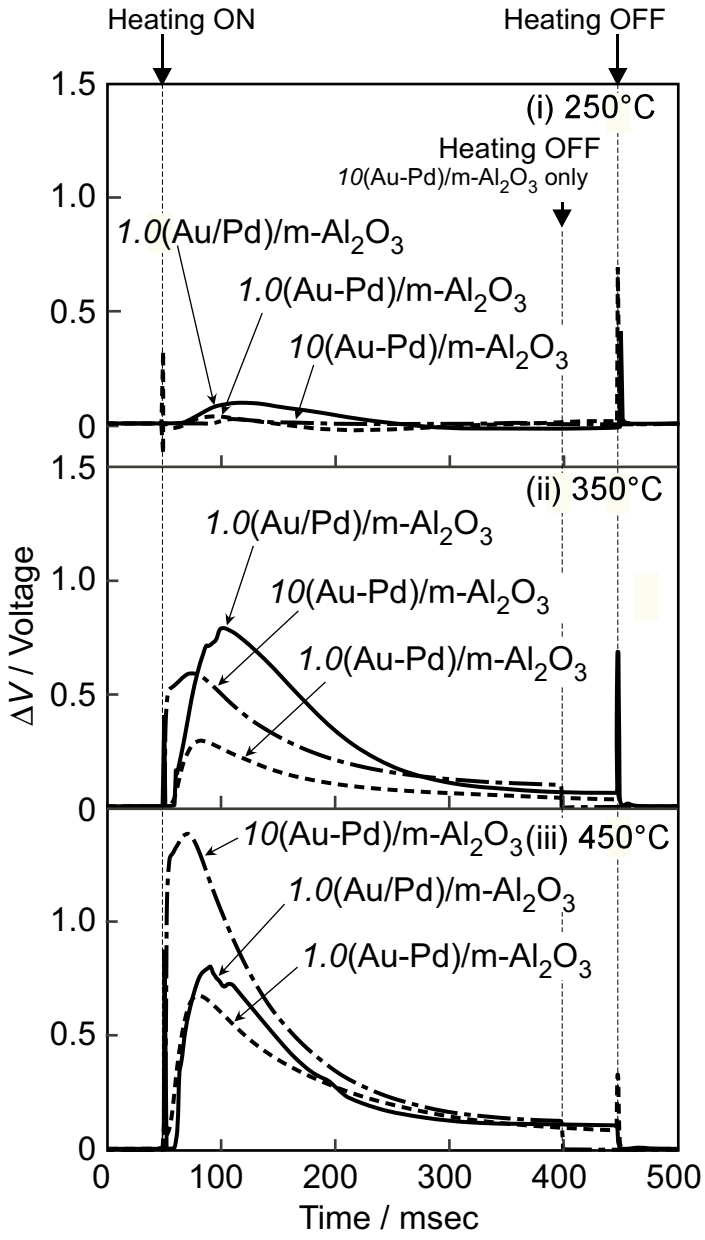

Fig. 9. Hyodo et al.

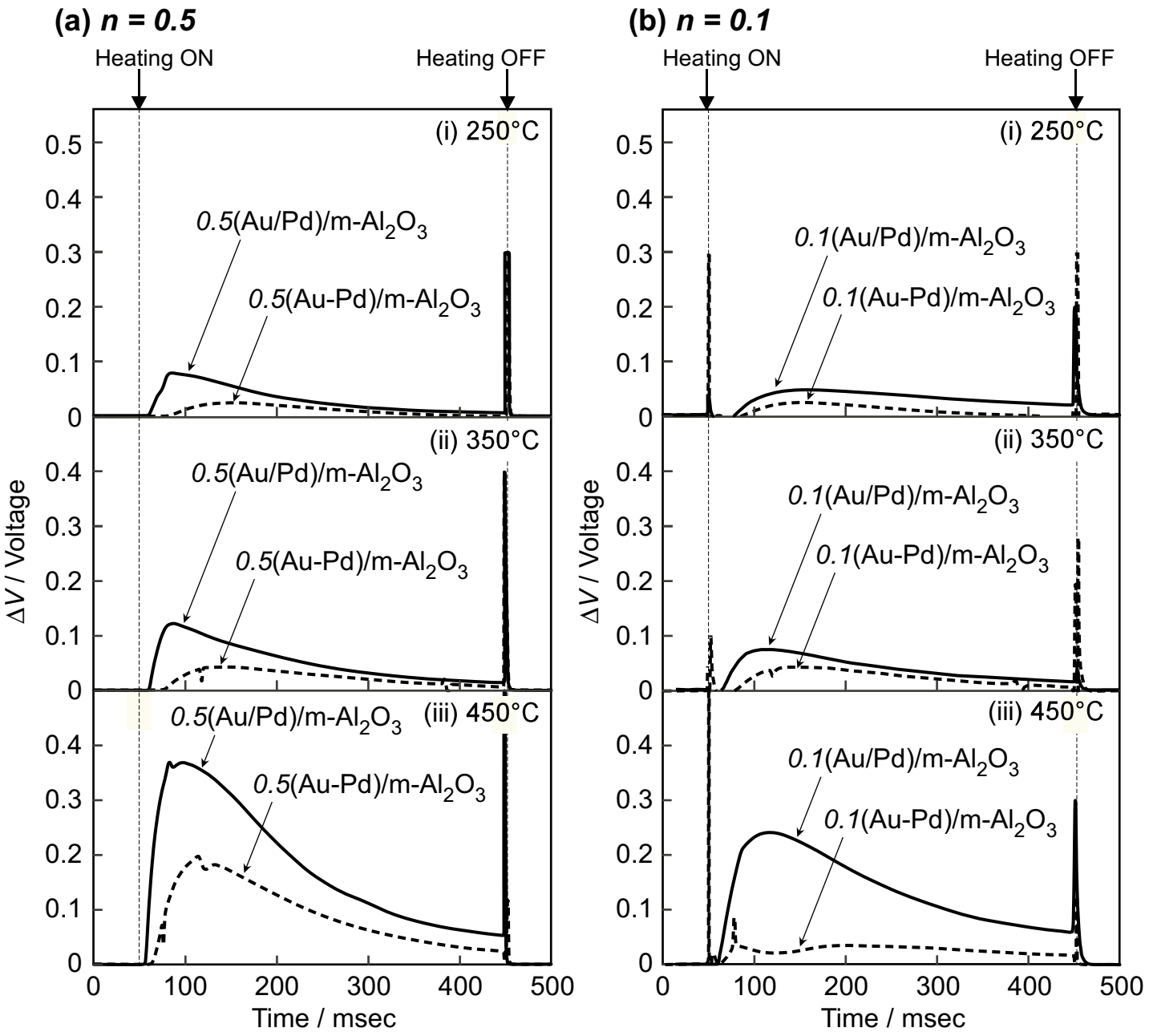

Fig. 10. Hyodo et al.

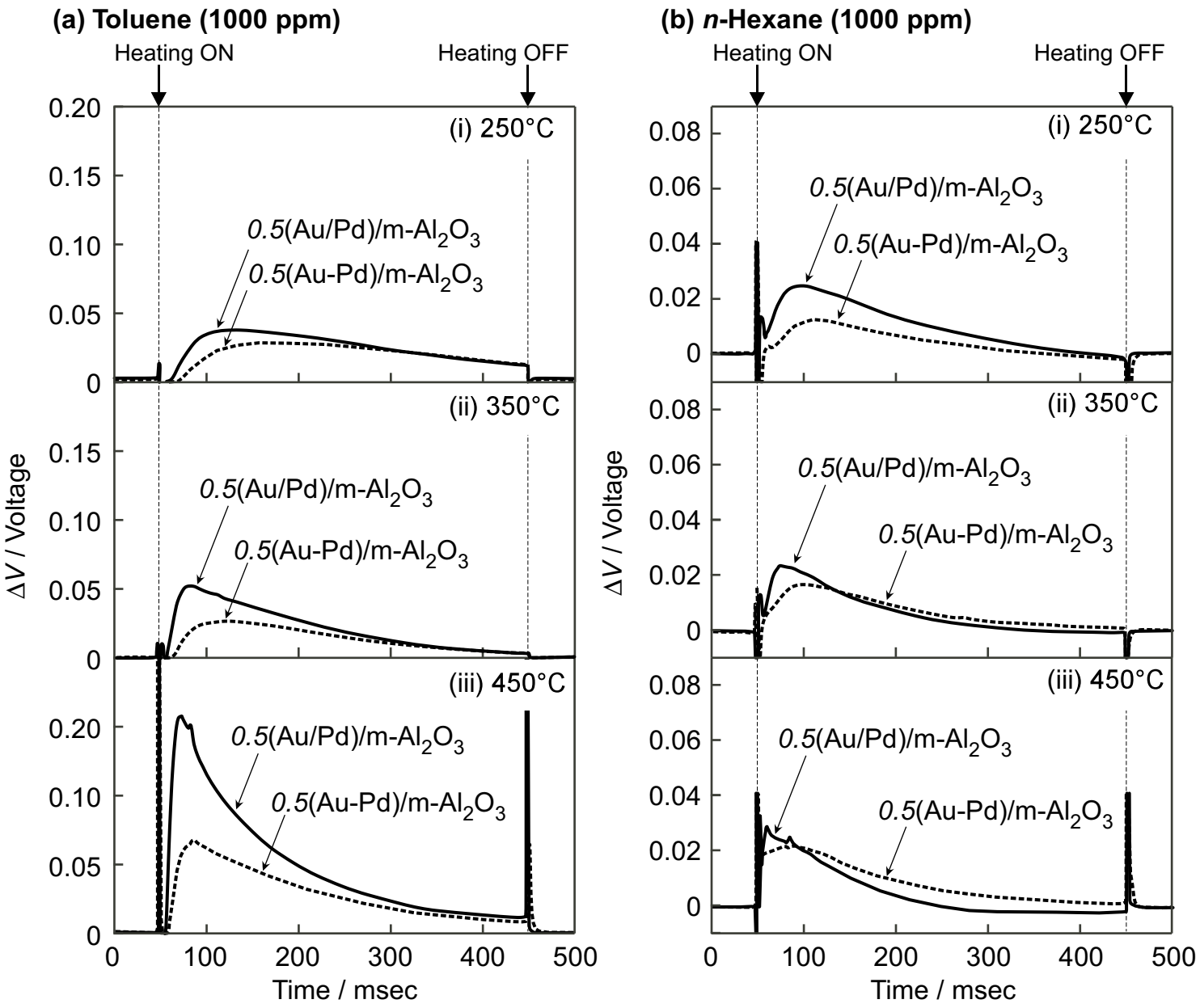

Fig. 11. Hyodo et al.

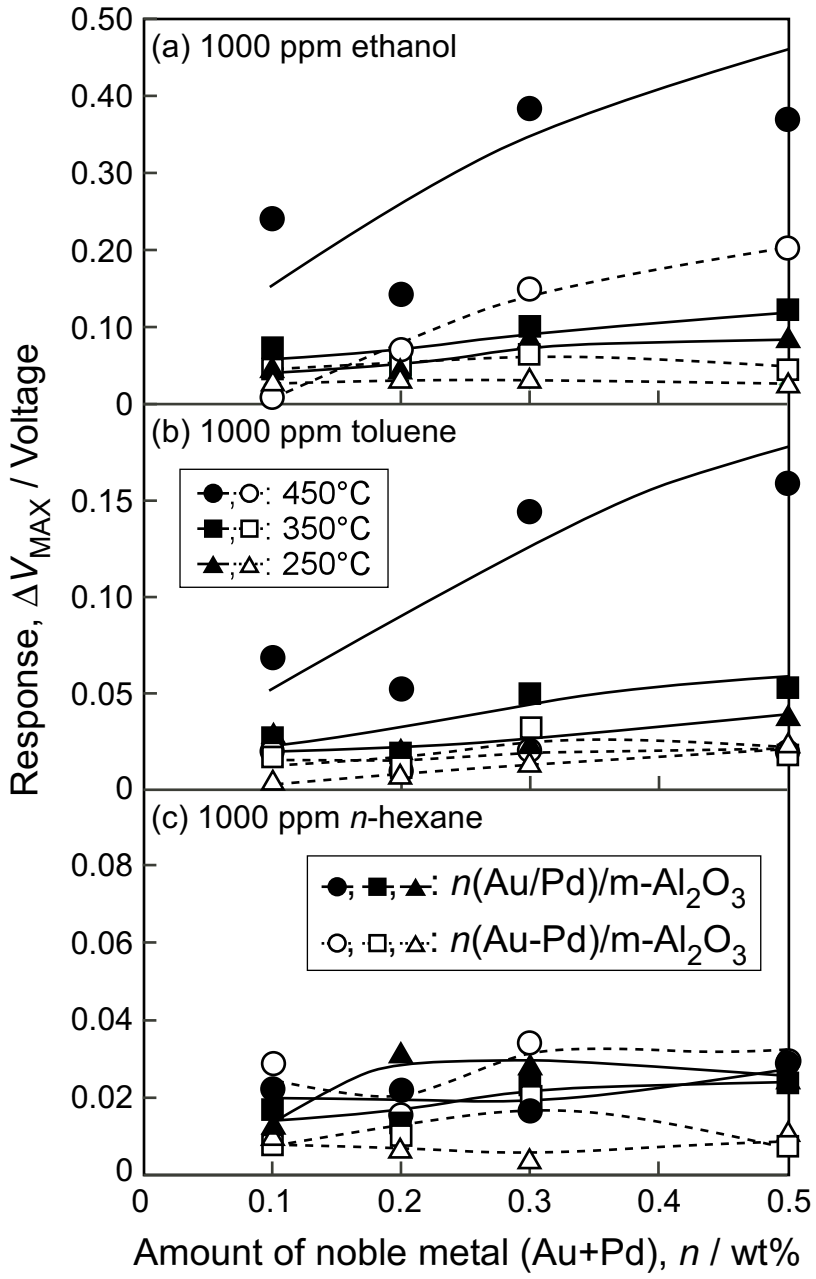

Fig. 12. Hyodo et al.

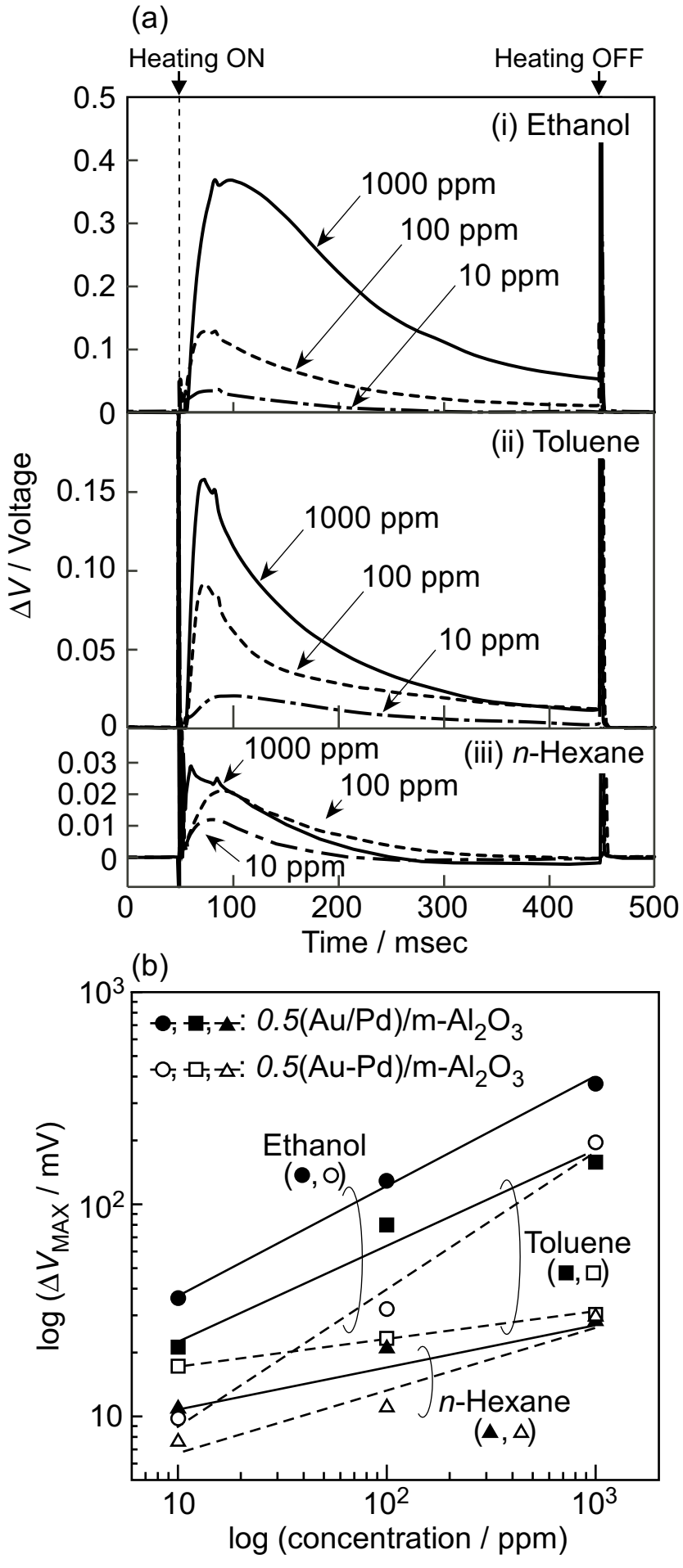

Fig. 13. Hyodo et al.